Longitudinal Awake Imaging of Deep Mouse Brain Microvasculature with Super-resolution Ultrasound Localization Microscopy

Yike Wang[1,2], Matthew R. Lowerison[1,2], Qi You[1,3], Bing-Ze Lin[1,2], Daniel A. Llano[1,4,5], Pengfei Song[1,2,3,5,*]

[1] Beckman Institute for Advanced Science and Technology, University of Illinois Urbana-Champaign, Urbana, IL 61801

[2] Department of Electrical and Computer Engineering, University of Illinois Urbana-Champaign, Urbana, IL 61801

[3] Department of Bioengineering, University of Illinois Urbana-Champaign, Urbana, IL 61801

[4] Department of Molecular and Integrative Physiology, University of Illinois Urbana-Champaign, Urbana, IL 61801

[5] Neuroscience Program, University of Illinois Urbana-Champaign, Urbana, IL 61801

[*]Corresponding Author: Dr. Pengfei Song (songp@illinois.edu)

Abstract

Super-resolution ultrasound localization microscopy (ULM) is an emerging imaging modality that resolves capillary-scale microvasculature in deep tissues. However, existing preclinical ULM applications are largely constrained to anesthetized animals, introducing confounding vascular effects such as vasodilation and altered hemodynamics. As such, ULM quantifications (e.g., vessel diameter, density, and flow velocity) may be confounded by the use of anesthesia, undermining the usefulness of ULM in practice. Here we introduce a method to address this limitation and achieve ULM imaging in awake mouse brain. Pupillary monitoring was used to confirm the awake state during ULM imaging. ULM revealed that veins showed a greater degree of vascularity reduction from anesthesia to awake states than did arteries. The reduction was most significant in the midbrain and least significant in the cortex. ULM also revealed a significant reduction in venous blood flow velocity across different brain regions under awake conditions. Serial *in vivo* imaging of the same animal brain at weekly intervals demonstrated the highly robust longitudinal imaging capability of the proposed technique. This is the first study demonstrating longitudinal ULM imaging in the awake mouse brain, which is essential for many ULM brain applications that require awake and behaving animals.

Introduction

Brain imaging provides invaluable insights into the underlying mechanisms that govern cognitive processes and neurological disorders. However, the complex nature of the brain presents significant challenges in directly and precisely measuring its functional properties[1]. In the field of neuroscience, there is a growing interest in utilizing imaging techniques to study the rodent brain, which serves as a valuable model for investigating brain function[2,3]. Brain imaging modalities for rodents encompass a wide range of techniques,

including but not limited to functional magnetic resonance imaging (fMRI)[4,5], positron emission tomography (PET)[6,7], one- and two-photon imaging[8,9], photoacoustic imaging[10,11], and more recently super-resolution ultrasound localization microscopy (ULM)[12]. ULM is uniquely capable of imaging micron-scale capillaries situated in deep tissue (e.g., at a depth of several centimeters). ULM can also be combined with the principles of functional ultrasound (fUS)[13–16] to image whole-brain neural activities at a microscopic scale[17]. The structural and functional imaging capabilities of ULM have opened new doors for numerous basic research and clinical applications that involve cerebral microvasculature[18–20].

At present, a key limitation associated with existing ULM brain imaging studies is the use of anesthesia, which induces profound alterations to cerebral blood flow (CBF) including changes in vessel size (e.g., diameter) and flow velocity[21]. As such, CBF measurements under anesthesia do not reflect the blood flow under the normal physiological state of the brain. In addition, anesthetics also have a significant attenuating effect on neural responses to sensory inputs, thereby impacting the neurovascular coupling process[22–27]. Therefore, brain imaging in the awake state is often preferred over under anesthesia in neuroscience research (e.g., fluorescence imaging[28], photoacoustic imaging[29,30], fMRI[5], PET[7], and fUS[31–34]). As ULM is gaining traction in many preclinical brain imaging applications, enabling ULM for awake animals has become essential to eliminate the confounding vascular effects of anesthetics and obtain accurate structural and functional cerebrovascular measurements.

Another challenge associated with preclinical ULM brain imaging is to conduct long-term, longitudinal studies, which are essential for tracking disease progression or therapeutic impacts for many neurological disease applications[35–37]. The key technical challenge for longitudinal ULM brain imaging is to find the same imaging plane and reconstruct consistent ULM images across different imaging sessions. Misalignment of imaging planes or tissue movement will undermine ULM imaging quality and result in inconsistent cerebrovascular quantifications. Although intact skull imaging has been shown to be feasible for short-term studies (e.g., over a few days)[19], long-term monitoring can be challenging because changes in skull properties over time (e.g., thickness and composition) could negatively impact ULM imaging quality. Currently there is a strong need for methodological developments to enable longitudinal brain imaging with ULM.

In this study we developed a method for awake and longitudinal ULM brain imaging in a mouse model to eliminate the confounding vascular effects of anesthesia and facilitate long-term monitoring of cerebral vasculature on the same animal. We constructed a head-fixed awake imaging platform and established a ULM image reconstruction metric to allow comparisons of ULM images acquired at different states of wakefulness (e.g., awake vs. anesthesia). Our method allowed detailed comparisons of local and global variations of the cerebral vasculature and blood flow under awake and anesthesia conditions. Detailed quantitative analysis of vessel diameter and blood flow velocity was performed. We also demonstrated robust longitudinal ULM brain imaging on same animals with high repeatability over multiple weeks. To the best of our knowledge, this is the first study that presents ULM brain imaging in awake mice under a longitudinal study setting.

Results

ULM brain imaging can be performed in awake mice.

To achieve motion-free and consistent ULM brain imaging, a head-fixed imaging platform with a chronic cranial window was used in this study. Pre-surgery handling and post-surgery habituation were employed to alleviate animal stress and facilitate awake imaging[34]. To further reduce animal anxiety and minimize tissue motion, a 3D-printed body tube was adopted[34] for animal immobilization (Fig. 1a). A headpost was implanted during cranial window surgery to fix the animal's head to the body tube. In this procedure, the skull was removed, and the brain tissue was protected using a polymethyl pentene (PMP) membrane, which was further protected by a layer of silicone rubber (Fig. 1b). Animals were imaged after one week of surgical recovery and head-fixation habituation. Prior to each imaging session, the silicone rubber was gently removed with forceps, and the transparent PMP membrane allowed detailed examination of the brain surface to ensure absence of tissue damage (Fig. 1c).

Contrast enhancing microbubbles (MBs) were administered intravenously via tail vein in this study (details provided in Methods). Isoflurane anesthesia was terminated right after MB injection, marking the beginning of the data acquisition (i.e., T = 0s). Mice were allowed to gradually regain consciousness. Throughout the awakening process, an infrared camera was used to monitor the pupil to provide a reference for the state of arousal[38] (Fig. 1d). Fig. 1e shows the change in pupillary area over time, which

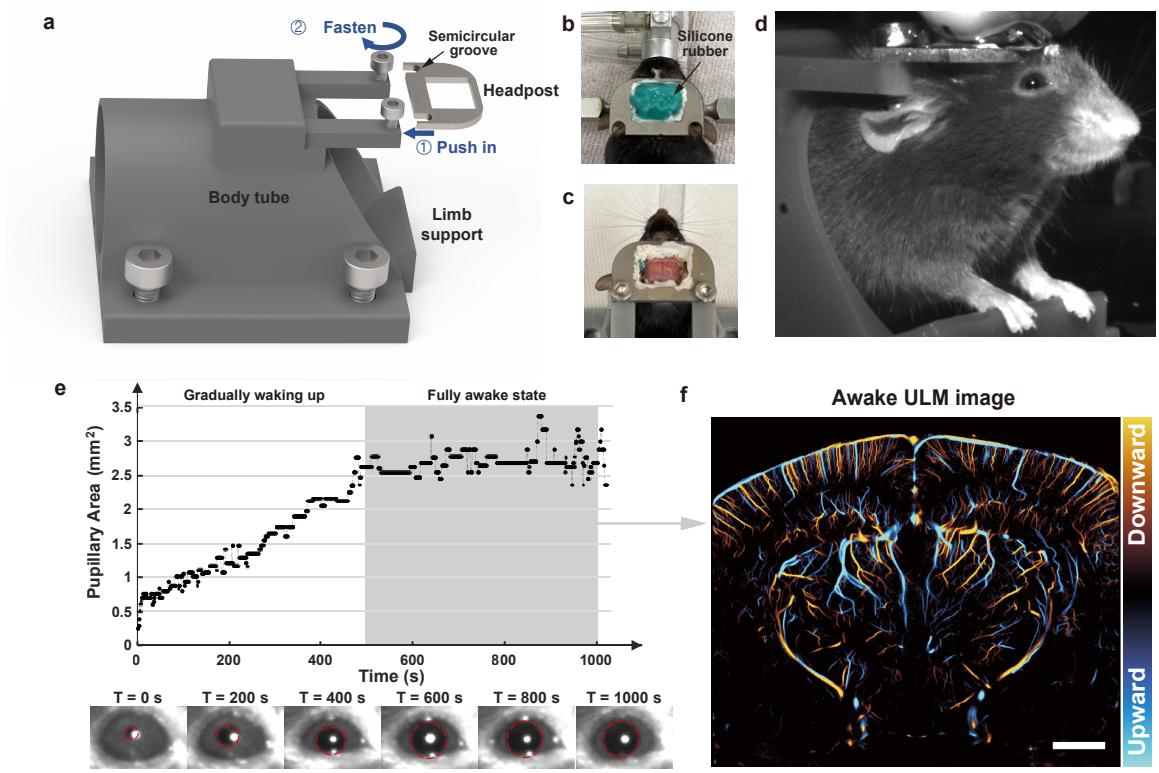

Fig.1 | Experimental setup for awake mice ULM brain imaging. **a,** 3D model of the body tube enabling rapid fixation of the headpost onto the tube. **b,** Top view photograph of the mouse after cranial window surgery, with the headpost protected by silicone rubber. **c,** Photograph taken after the post-surgery recovery, with the removal of the silicone rubber protection. **d,** Image captured by the camera positioned in front of the mouse during the imaging session. **e,** Change of the pupillary area over time, after microbubble injection (T = 0s), along with magnified portion of the pupil photo in **d** at six time points (T=0, 200, 400, 600, 800, and 1000 second). Pupil is outlined with red dashed circle. **f,** Awake ULM image obtained from data collected during a fully awake state, as indicated by the gray shaded area in **e**. (scale bar: 1 mm)

reveals a gradual enlargement of the pupil after the cessation of anesthesia. To ensure that ULM accurately captures the cerebrovascular characteristics in the awake state, ULM reconstruction only used the data that acquired after the animal reached full pupillary dilation. Ultrafast plane wave imaging data were collected for ULM reconstruction (details provided in Methods) and a representative awake ULM brain image is presented in Fig. 1f.

Microbubble count serves as a quantitative metric for awake ULM image reconstruction.

Due to the stochastic nature of MB localization and fluctuations of MB concentration in the blood stream, it is challenging to compare ULM images acquired at different states of wakefulness with different cerebral blood flow conditions. Therefore, to obtain complete, fully saturated ULM images under different physiological conditions and MB concentrations, we used MB count as a measure of vessel saturation to

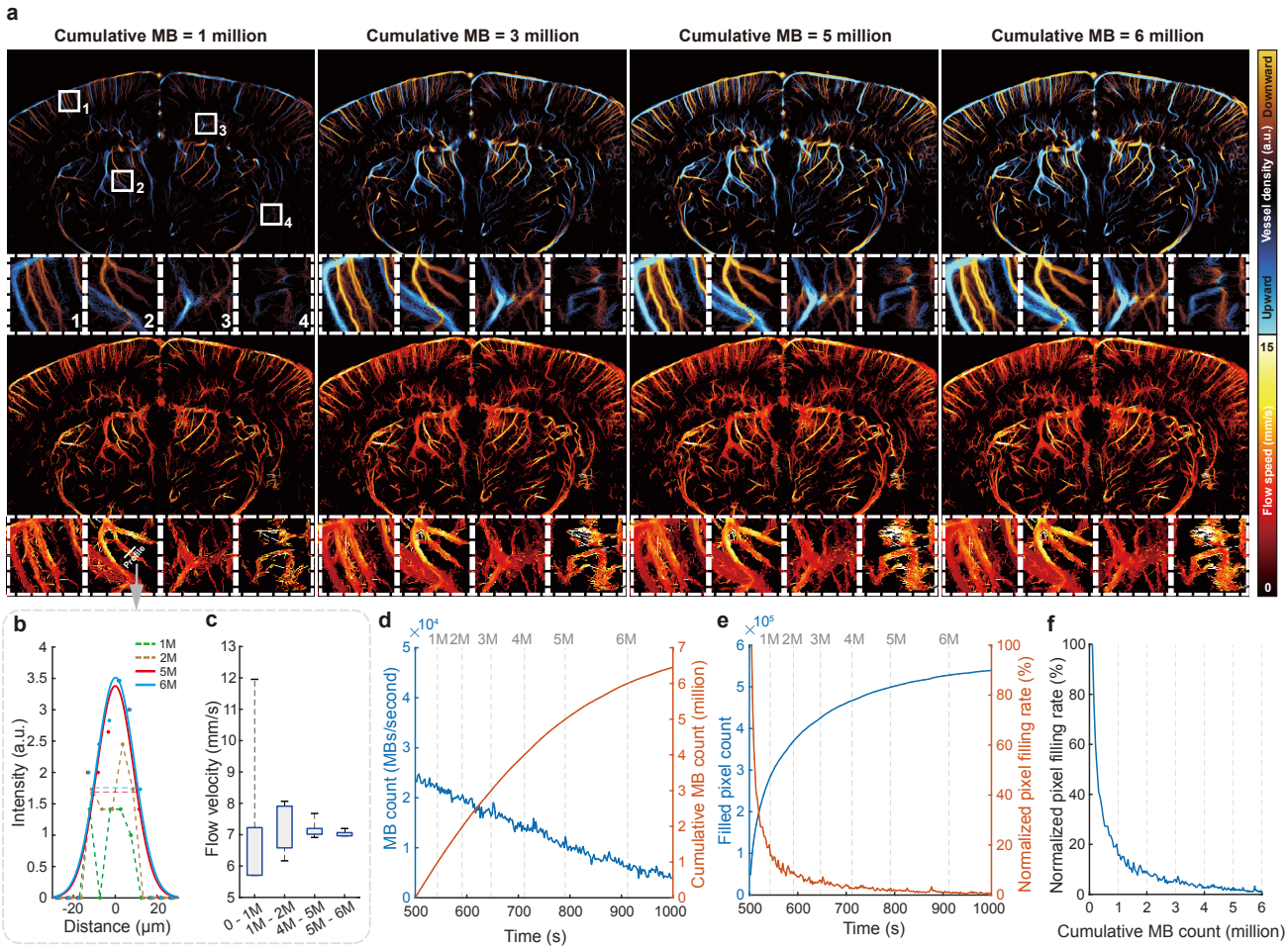

Fig.2 | Data processing standards for awake mice ULM imaging. a, ULM directional vessel density maps and flow velocity maps at cumulative MB counts of 1, 3, 5, and 6 million. **b,** Vessel profile from the density map at cumulative MB count of 1, 2, 5, and 6 million. The profiles of 5M and 6M MBs are fitted by a Gaussian curve, and the diameter of the vessel is estimated by the Full Width at Half Maximum (FWHM). **c,** Variation of measured mean velocity at the profile in the ULM flow speed map calculated at different cumulative MB count. **d,** Time courses of MB count in each second (blue curve) and the cumulative MB count (orange curve) starting from T = 500s. The vertical gray dashed lines indicates the time points when the cumulated MB count reaches 1, 2, 3, 4, 5, and 6 million. **e,** Time courses of saturation level of the ULM image (blue curve) and the filling rate of pixels (orange curve). The filling rate is calculated by taking the derivative of the filled pixel count, and then normalized to the initial filling rate at the beginning of ULM reconstruction (T = 500s). **f,** Relationship between pixel filling rate and cumulative MB count, eliminating the time axis by plotting the orange curves from **d** and **e** together.

determine the completeness of ULM reconstructions. To ensure high quality ULM imaging, only MBs persistently observed in more than 10 consecutive frames (10 ms) were considered as effective MB signals that were utilized for ULM image quantification.

Fig. 2a compares the ULM directional vessel density maps and flow speed maps obtained with 1, 3, 5, and 6 million MBs. No obvious changes of vessel density or flow speed can be observed between 5 and 6 million MBs, indicating a complete ULM reconstruction with saturated vessel fillings at 5 million MB count. To quantitatively confirm ULM image saturation, a vessel profile was selected for further analysis. Fig. 2b displays the profile of the vessel reconstructed at various MB counts. When the MB count was low, the reconstructed blood vessels were not fully filled (green and brown curves) and the vessel diameter was difficult to estimate due to the incomplete profile. When the blood vessels were saturated with MB localizations at high MB count, vessel diameter was measured by the full width at half maximum (FWHM) of the Gaussian-fitted vessel profile. The plots (Fig. 2b) clearly indicate that the vessel diameter stabilized beyond 5 million MB count. Fig. 2c presents the changes in mean velocity measurement using different cumulative MB count, which starts with large variance and gradually converges as the MB count increase. At 5 million MBs, flow velocity estimation becomes stable with small variances, and does not exhibit obvious differences from the measurement with 6 million MBs. This result is in good agreement with previous studies where vessel velocity measurements stabilize as the MB count grows[39].

Fig. 2d shows a clear trend of decreasing MB concentration in the blood stream and increasing cumulative MB count with time. Fig. 2e demonstrates a flattened vessel saturation curve and a rapidly reducing vessel filling rate, which is typical for ULM reconstruction[39]. The pixel filling rate dropped below 5% of the initial rate after 300 seconds of ULM data accumulation (T = 800 s), indicating ULM image saturation. Fig. 2f further examines the relationship between the pixel filling rate and the cumulative MB count, which is independent of data acquisition time. The pixel filling rate at 5 million cumulative MBs is always below 5% of the initial rate for each experiment, ensuring image saturation. In summary, all the quantitative measurements indicate that ULM images obtained using the proposed metric (i.e., 5 million MBs) were complete and can be used to consistently measure cerebral vascular properties such as vessel diameter and blood flow velocity. All subsequent ULM images in this study were produced using this criterion.

ULM reveals detailed cerebral vascular changes from anesthetized to awake for the full depth of the brain.

Fig. 3 presents a comparison of ULM directional vessel density maps and flow velocity maps in awake and anesthetized states for three different coronal planes from three animals. ULM data under anesthesia was acquired prior to each awake imaging session (See Methods part for details). Four regions of interest (ROIs) were selected within each imaging plane to provide detailed comparisons. When comparing directional vessel density maps, ULM demonstrates a global vascularity reduction in the awake state. The reduction is also clearly observed in magnified local regions especially for regions 5, which encompasses the pretectal region. In addition to reduced vascularity, ULM also clearly reveals decreased vessel diameter which reflects vasoconstriction after the animals woke up (e.g., white arrows in regions 1, 3, and 6, corresponding to the thalamus, cortex and midbrain/cortex overlap region). Focusing on ULM flow speed maps, a global reduction in flow speed can be clearly observed when transitioning from anesthetized to awake. Regional maps further revealed the significant flow speed reduction for most of the vessels throughout the brain (e.g., blue arrows).

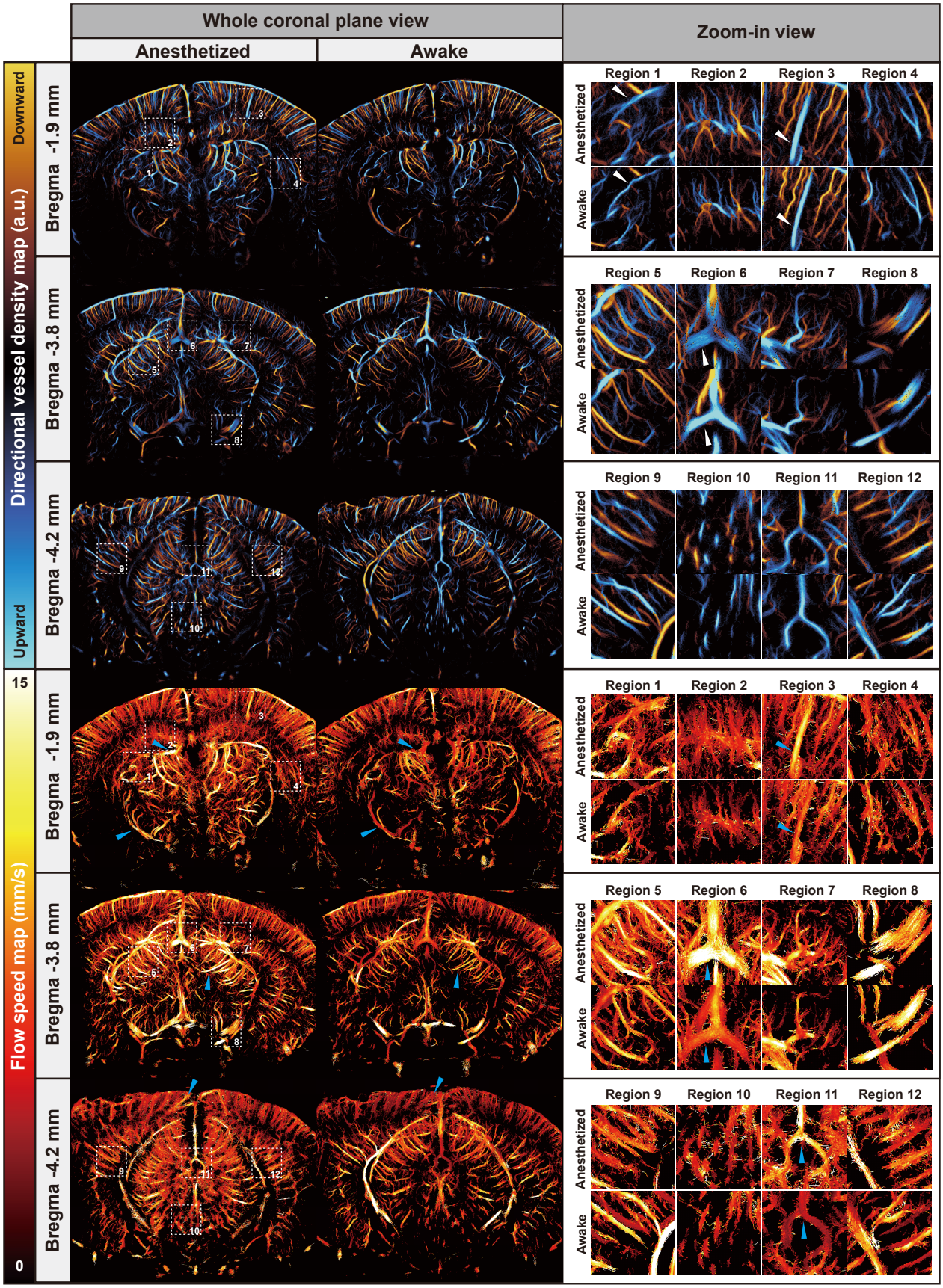

Fig.3 | Comparison of ULM images in anesthetized and awake states. Three coronal planes are selected at Bregma - 1.9mm, Bregma - 3.8mm, and Bregma - 4.2mm. The upper panel shows the comparison of directional vessel density maps, while the lower panel shows the comparison of flow velocity. Four regions of interest (ROIs) are selected within each coronal plane (indicated by white dashed boxes in the whole-plane view of the vessel density map) for zoom-in comparison.

To investigate the influence of isoflurane on different types of vessels, we then combined the vessel morphology and flow direction information from the ULM images to classify the cerebral vasculature into arteries, veins, and capillaries (Fig. 4a, details provided in Methods). Briefly, ULM images differentiate MB tracks into upward flow (towards the probe) and downward flow (away from the probe) based on the Doppler frequency shift[40]. With this information, the vessels flowing from the main stem to the branches were classified as arteries, while those flowing from the branches to the main stem were classified as veins. Fig. 4b presents an example of a vein that underwent marked vasoconstriction (from a diameter of 135.5 µm to 72.1 µm) and significant flow speed reduction after the animal woke up. Similar cases of a cortical vein (Region 3 in cerebral cortex, reduced from 50.6 to 36.3 µm) is presented in Fig. 4c. The combination of a reduced flow speed and decreased vessel diameter indicates a reduced blood flow volume through the vessel, which is consistent with previous studies[21,23]. Interestingly, isoflurane showed varying effects on veins and arteries. An adjacent artery-vein pair was selected to calculate the diameter and flow speed distribution along the cross-section profile (Fig. 4d). The selected artery did not exhibit significant diameter change (from 36.5 µm to 31.8 µm) or flow speed reduction in the awakening process (Fig. 4e), while the vein demonstrated a substantial alteration in diameter (from 45.9 µm to 23.9 µm) as well as a significant reduction in velocity (Fig 4f). Other investigations have also demonstrated that arteries and veins respond differentially to anesthetics[21,41,42].

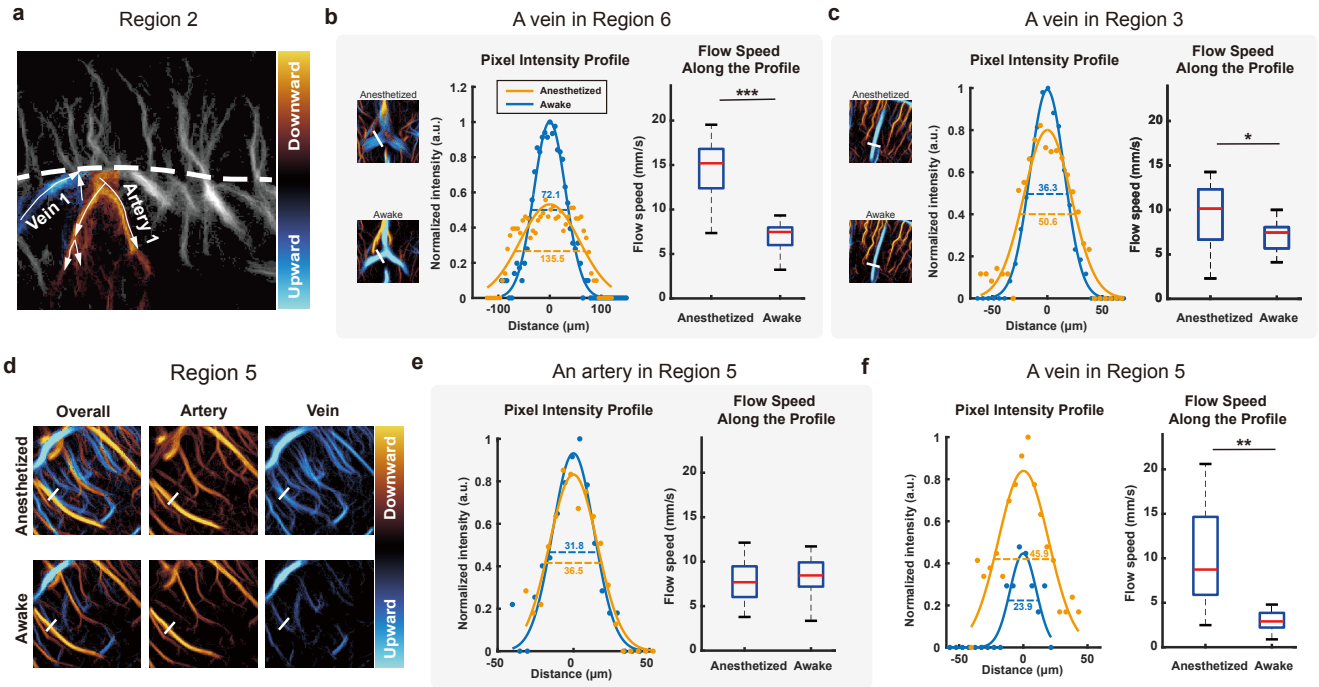

Fig.4 | Quantitative analysis of differences in individual vessel between anesthetized and awake states. a, Schematic diagram illustrating the differentiation between arteries and veins based on the stems and branches of the vessels, combined with the flow direction information obtained from ULM. For example, Artery 1 is identified as an artery because it exhibits downward flow, indicating the stem-to-branch direction. Vein 1 can also be labeled using the same criteria. **b,c,** Profile analysis for a selected vein along the white line in Region 6 (corresponding to **b**) and Region 3 (corresponding to **c**), respectively. Differences between anesthesia and awake states are compared. Gaussian fitting of the intensity values along the profile is performed to measure the vessel diameter, and the flow velocity distribution along the profile is compared in the boxplot. **d,** ULM images of an adjacent artery and vein within Region 5 in **Fig 3**, with profiles drawn along the white lines for the artery and vein at the same position. **e,f,** Comparison of vessel diameter and flow velocity obtained from artery profiles (corresponding to **e**) and vein profiles (corresponding to **f**). Significance analysis is conducted using a T-test (*: $p<0.05$, **: $p<0.01$, ***: $p<0.001$).

Statistical analysis validates the increase in blood flow induced by anesthesia.

Statistical analysis was performed for arteries and veins in distinct brain regions. Different ROIs in the cortex (CTX), hippocampal formation (HPF), thalamus (Thal) and midbrain (MBr) were selected from three coronal planes (Supplementary Fig. 1). Fig. 5a-c illustrate the percentage change in vessel diameter (quantified by FWHM) from anesthesia to the awake state. Overall, there was a reduction in vessel diameter in most brain regions. Because many vessels such as the veins shown in Fig. 4d became invisible in the awake state, the total vessel area (i.e., measured by number of pixels representing vessels) was

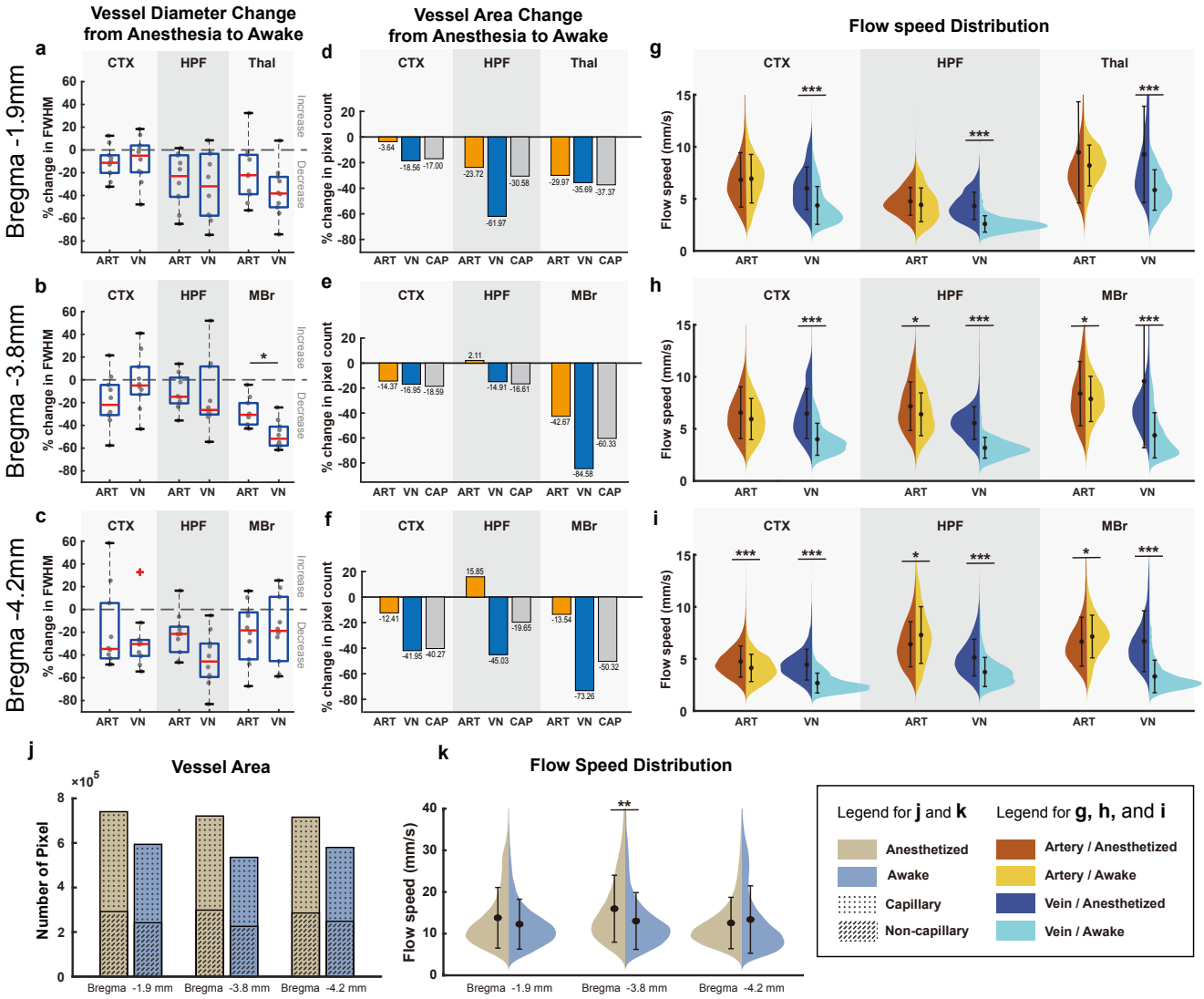

Fig.5 | Quantitative analysis of differences between anesthesia and awake states in different brain regions. a,b,c, Percentage changes in vessel diameter from anesthesia to awake state in different brain regions, from cortex, hippocampus, and brainstem. Selected vessels for measurement are indicated in Supplementary Fig. 1. Bregma -1.9 mm corresponds to **a**. Bregma -3.8 mm corresponds to **b**, and Bregma -4.2mm corresponds to **c**. The red cross in the boxplot represents outlier. **d,e,f,** Percentage changes in vessel area from anesthesia to awake state. Vessel area is calculated from the pixel count within the ROIs. **d-f** correspond to the three sections in **a-c**, respectively. **g,h,i,** Violin plots showing the distribution of flow velocity values measured in all pixels within the ROIs of each brain region, comparing anesthetized and awake states. The y-axis represents the measured flow velocity values, while the width represents the corresponding probability density. **g-i** correspond to the three sections in **a-c**, respectively. **j,** Comparison of pixel count in the ULM density map between anesthesia and awake states for all the three different sections. Pixels with intensities below 2 are labeled as capillaries. **k,** Violin plots illustrating the distribution of flow velocity measured in all pixels within the entire coronal sections. Significance analysis is performed using a T-test (*: $p<0.05$, **: $p<0.01$, ***: $p<0.001$). ART: artery, VN: vein, CAP: capillary, CTX: cortex, HPF: hippocampus formation, Thal: Thalamus, MBr: Midbrain.

utilized as another quantitative metric to evaluate vascular changes. Fig. 5d-f shows the percentage change in vessel area for arteries, veins, and capillaries within each ROI. Most brain regions exhibited a reduction in vessel area, except for a slight increase in arterial pixels in the HPF. Notably, reductions associated with venous area were more substantial compared to those in arteries (especially for MBr region in Fig.5e, f and for HPF region for Fig. 5d). As for the comparison between brain regions, midbrain showed relatively more vessel area reduction overall. CTX showed the smallest amount of vessel area reduction especially for the most rostral imaging plane (reduction of 3.64% for Bregma -1.9mm). This work is consistent with a previous fMRI study, where it was also observed that isoflurane-induced cerebral hyperemia was not most pronounced in the cerebral cortex compared with other deeper brain regions[43].

CBF changes caused by anesthesia was further indicated by flow speed measurements (Fig. 5g-i). Notably, along with the vessel diameter and vessel area reductions for veins across different brain regions, the venous blood flow velocity was also significantly lower in the awake state ($p<0.001$), indicating an overall reduction of venous blood flow volume post anesthesia. Reduction in arterial blood flow velocity was mostly insignificant except for the most caudal imaged plane (Bregma -4.2mm). Extending the analysis to the entire coronal plane rather than regional analysis, Fig. 5j indicates a global reduction in vascularity post anesthesia, and both capillary and non-capillary regions contributed to the decrease in blood flow. Global flow velocity distribution (Fig. 5k) did not exhibit a consistent trend across the three planes, which may be because of varying compositions of large arteries and veins in each section. In addition, it is worth noting that the flow speed measurement in Fig. 5g-i examines smaller vessels (velocity distribution at 10mm/s). There are more large vessels (flow velocity between 20-40mm/s) in the analysis of the entire coronal plane. While small vessels dominate more area in the 2D plane compared to large vessels, the latter have a greater capacity to regulate global CBF. Considering the relationship between vessel area, flow speed, and CBF, although the global flow speed remains largely the same, there is a decrease in vessel area. This decrease suggests a reduction in the overall CBF.

In summary, statistical analysis revealed a decrease in individual vessel diameter, total vessel area, and blood flow velocity (particularly in venules) after awakening. These findings align with existing research, indicating higher blood perfusion during isoflurane anesthesia[21,41,42,44,45].

Awake ULM imaging demonstrates high consistency in longitudinal imaging across different weeks.

Longitudinal awake ULM brain imaging was feasible using the surgical and imaging techniques presented in this study. Fig. 6a presents the results of awake brain imaging performed on the same brain region over three consecutive weeks. Three ROIs at different depths were selected to compare microvessel reconstruction across different time points. Fig. 6a demonstrates a high level of consistency in both directional vessel density maps and flow speed maps obtained from the three imaging sessions, although some minor discrepancies were observed (e.g., the vessel indicated by the green arrow in Fig. 6a). The inconsistency could potentially be attributed to physiological variation and/or slight misalignment.

To quantitatively evaluate the accuracy of ULM feature extraction in the longitudinal studies, six blood vessels in ROI 1 from the cortex were selected to measure the diameter. For each week, the FWHM of the Gaussian fitted profile was measured at the same locations in the ULM images (marked in the zoom-in view of Region 1 in Fig. 6a). The results demonstrate small variation in the measured vessel diameters across the weeks, with standard deviations of 5.6%, 4.2%, 4.6%, 2.0%, 1.3%, and 3.2% relative to the mean diameter respectively (Fig. 6b). These standard deviations are significantly lower than the impact of

vasodilation induced by anesthesia on vessel diameter (Fig. 6c). To evaluate the consistency of blood flow velocity measurements, we selected one blood vessel from each of the three ROIs. Fig. 6c shows the flow speed comparisons of the three selected vessels across different weeks. Analysis of variance (ANOVA) and post hoc multiple comparison procedures (Tukey's test) showed no significant differences among any of the weekly measurements.

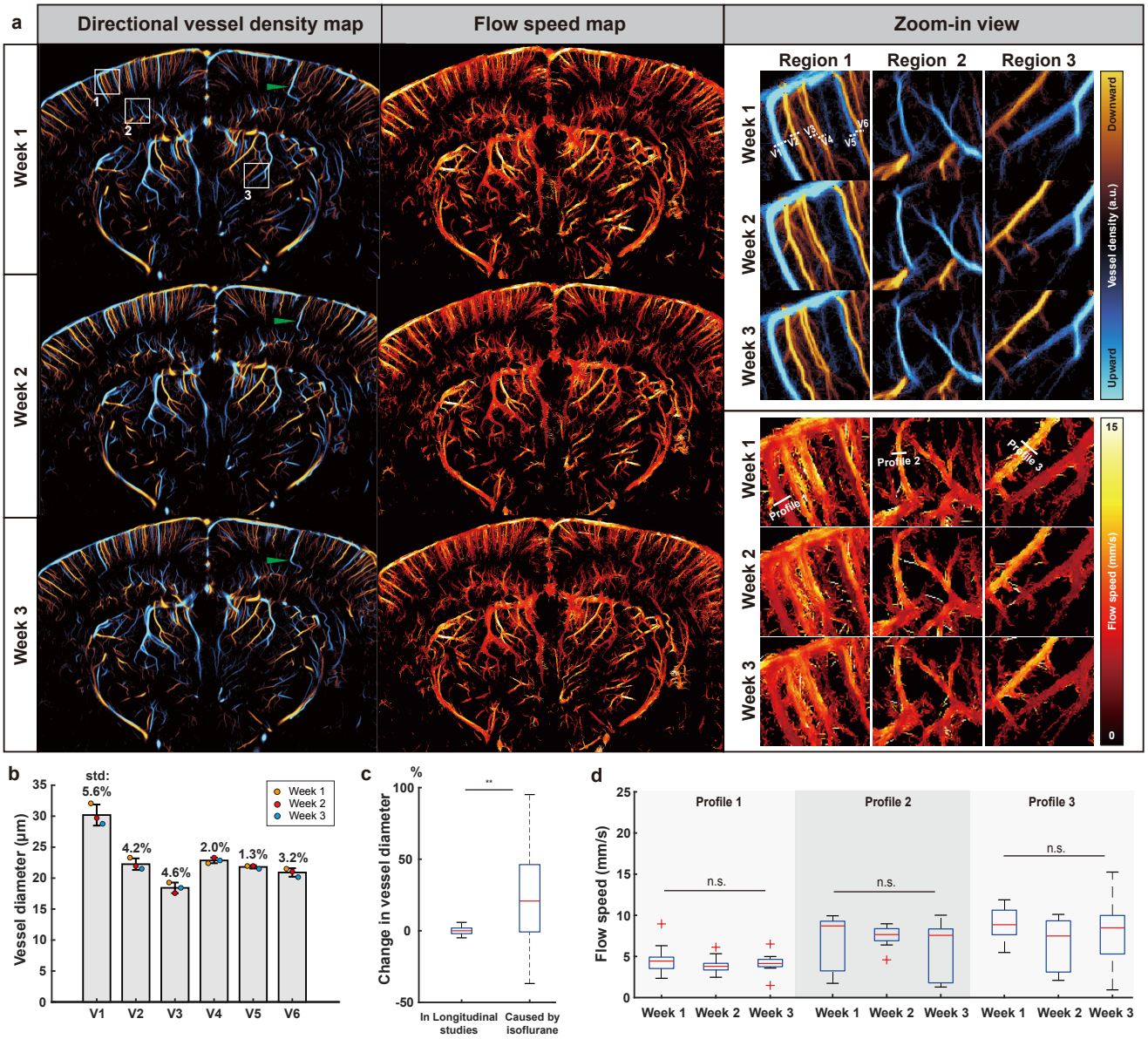

Fig.6 | Longitudinal awake ULM imaging results on the same coronal plane for three consecutive weeks. a, Comparison of ULM directional vessel density maps and flow speed maps acquired over three weeks, with a selected region of interest (ROI) magnified for comparison in the cortex, hippocampus, and brainstem (white boxes). **b,** Measurements of vascular diameters in six cortical vessels (marked in the zoom-in view of Region 1 in week 1. **c,** Comparison of vessel diameter changes between longitudinal awake imaging and anesthetized imaging. In the longitudinal study, percentage changes were calculated for all the six vessels in **b** with respect to the average diameter of each vessel. In anesthetized imaging, percentage changes under anesthesia relative to awake conditions were calculated from all the marked cortical vessels in Supplementary Fig. 1. Significant difference was calculated by t-test (p=0.0032). **d,** Flow velocity measurement results of three different vessels (as indicated by the profile in the flow speed map of week 3, with significance analysis in data distribution through one-way ANOVA and multi-compare (Significance level: 0.05). (n.s. non-significant). The red cross in the boxplot represents outlier.

Discussion

In this study, we introduced a method for performing ULM brain imaging in awake mice under a longitudinal study setting. Our method enabled high-resolution imaging of deep cerebral micro-vasculature with the animal under awake state. We translated the awake imaging techniques previously described in fUS[34] to our study to enable awake ULM, and established a quantitative metric for ULM image reconstruction. Based on the setup above, we studied CBF changes induced by anesthesia, which aligned well with literature. Isoflurane has been shown to increase vascular diameter and CBF in mice, as validated by multiple imaging modalities including optical coherence tomography[41], photoacoustic microscopy[42], two-photon microscopy[44], and laser speckle imaging[21,45]. These effects have also been validated in larger animal models such as rats[43], dogs[46], and marmosets[47]. In human, vasodilation and increased CBF caused by volatile anesthetics such as isoflurane have also been reported[23].

Statistical analysis from Fig. 5 shows larger vascular diameter and higher vascular density under anesthesia. These findings are consistent with existing research[21,41,42,44,45]. It is worth noting that although our data indicate a global elevation of CBF under isoflurane anesthesia, individual vessels exhibit large discrepancies in behavior. For example, the vessel at the right lower corner from Region 9 in the HPF (Fig. 3) shows almost no blood flow during anesthesia but then exhibits high vessel pixel density after awakening. The wide range of vessel behaviors were also previously reported in literature[21,47]. Our results indicate that awake ULM imaging has ample spatial resolution and imaging depth of penetration to resolve individual vessel variations down to micron-sized vessels deep into the brain. This is a unique capability that is not available from other biomedical imaging modalities.

Increased blood flow velocity induced by isoflurane has also been reported by other studies[41,42]. However, previous research presented different speculations on the predominant factor contributing to the increase in CBF induced by anesthesia, specifically whether the increase is attributed to vasodilation or increase in blood flow velocity[21]. One study found significant changes in both blood flow and vessel diameter but minor changes in flow velocity, suggesting that the increase in blood flow was largely driven by vasodilation[41]. Conversely, another study drew the opposite conclusion[21]. Benefitting from the large field of view (FOV) of ULM and its capability to directly quantify microvascular blood flow velocity, we can make a more comprehensive inference regarding the relationship among the changes in vessel diameter, flow speed, and flow volume from anesthetized to awake states. For arteries, the change in blood flow velocity is not significant, indicating that the alteration in blood flow may be primarily due to vasodilation instead of velocity change. Isoflurane causes vasodilation by acting on the ion channels (e.g., potassium channel) of smooth muscle[46], which is more abundantly found in arteries than in veins. In the case of veins, which do not actively dilate or constrict, their vessel diameter and blood flow variations are more likely controlled by passive mechanisms. Fig. 5 reveals significant differences in flow velocity of veins between anesthesia and awake state, suggesting that the changes in flow velocity may have a greater impact on venous blood flow volume compared with arterial volume.

The differences in cerebral vasculature between anesthetized and awake states observed using ULM are also in agreement with other studies[21,41,42,45]. However, previous studies mostly used optical imaging techniques, which have limited penetration depth and can only observe surface pial vessels in the cortex. Some other studies using fMRI can detect deeper CBF changes in the whole brain, but they do not provide insights about small vessel blood flow variations due to insufficient spatial resolution[43]. As a bridging imaging modality between MRI and optical techniques, awake ULM enables observations of detailed

microvascular variations induced by anesthesia across the whole depth of the brain, which provides complementary information to existing biomedical imaging modalities.

Our proposed method enabled long-term, repeatable longitudinal brain imaging, which addressed a key issue of conventional ULM imaging and could be useful for many preclinical applications. However, there are still some limitations in this study. First, the differentiation between arteries and veins is based on blood flow direction and the relationship between branches and stems. Finding the branches of all the vessels, however, can be difficult since the FOV is confined to the coronal plane and the branches of the vessels are not necessarily within the 2D FOV. We can only classify vessels based on the assumption that all arteries flow in the same direction and all veins flow in the opposite direction within a small region of the brain (e.g., the circled regions in Supplementary Fig. 1). Although this assumption is based on 3D representations of the cerebral vascular network[48–52], inaccurate artery and vein classification remains possible, which is one of the limitations of 2D imaging. With 3D ULM[53,54], a whole-brain vascular network can be generated, facilitating more comprehensive and accurate classification of vessel types. Meanwhile, 3D ULM also helps to alleviate the issue of identifying the identical coronal plane for longitudinal imaging, which requires careful manual alignment in 2D ULM to ensure consistency.

Tissue motion is also a critical concern of ULM imaging. Benefiting from the robust head-fixing protocols and successful habituation, we did not observe significant motion artifacts in the ULM images. Nevertheless, we still employed the correlation method to register the ULM images[55] in order to remove subtle tissue movement and improve the ULM image quality. This method preserves the maximum fidelity for the MB tracks, but may not be adequate for non-rigid motion. Meanwhile, with 2D imaging, we cannot correct for out-of-plane motion, which necessitates 3D imaging. In the future, 3D motion correction techniques that account for complex tissue motions and are computationally efficient need to be developed for awake and longitudinal ULM imaging.

In this study we established a ULM reconstruction standard (e.g., 5 million MB counts) to facilitate quantitative comparisons among ULM images acquired from different physiological states and time points. There are also possible alternatives for ULM image normalization. For example, different ULM images can be normalized to have the same pixel filling rate, which ensures consistent ULM image saturation. However, our proposed method of using the same number of cumulative MB count for normalization enables the analysis of blood flow distribution across different brain regions from a probabilistic perspective. This facilitates a more equitable comparison of brain perfusion with the same amount of blood flow at different states of wakefulness.

Longitudinal brain imaging in the awake state offers a promising tool for neuroscience research as it not only avoids the confounding effects of anesthesia on cerebral vasculature, but also enables observations of intrinsic dynamics of the vasculature within the same subject, minimizing potential sources of bias associated with inter-subject variability. In the future, this technique is expected to be further integrated with disease models to study the changes in cerebral vasculature during the development of diseases. Also, this technique can be further combined with the latest functional ULM (fULM) studies[17] to allow awake fULM imaging. Our study laid the foundation for these studies with awake fULM, which is expected to improve the sensitivity of conventional fULM techniques because hemodynamic responses are much stronger in the awake state than in anesthesia[25–27].

Methods

Animal preparation

Six healthy female C57 mice (8-12 weeks) were used for this study. All experimental procedures were conducted in accordance with the guidelines set by the University of Illinois Institutional Animal Care and Use Committee (IACUC Protocol number #22165). The animals were housed in an environment with a 12-hour light/dark cycle and had free access to food and water. Prior to the cranial window surgery, the mice were kept in group housing, and they were individually housed post-surgery.

Pre-surgery handling

A week before performing the cranial window surgery, the animals underwent tunnel handling, a procedure shown to significantly reduce the levels of anxiety in mice[56,57]. Specifically, a commercially available polycarbonate mouse transfer tube (TRANS-TUBE 130X50MM, Braintree Scientific, Inc.) was used for the initial three days. The mice were encouraged to enter the tube from their cage, after which the tube was lifted, allowing the mouse to remain inside for 30 seconds. The mouse was then returned to its cage for free movement for one minute, before a second identical tunnel handling was carried out. This procedure was done twice daily. Approximately three days into this routine, the mice were accustomed to the tunnel handling method. The animals were then picked up using the commercial tunnel, and then a 3D-printed body tube was attached to the other end of the tunnel. The mice were allowed to enter the body tube voluntarily. Subsequently, the body tube was utilized for handling the mice in the following 5 days as a replacement for the commercial tunnel.

Cranial window surgery

The entire procedure closely followed a previously published protocol[34]. To minimize brain swelling, the animal received an intraperitoneal injection of Dexamethasone (0.5 mg/kg body weight). The mouse was anesthetized by inhalation of isoflurane (3% for induction and 1%-1.5% for maintenance). After confirming that the mouse was insensate, the head of the animal was fixed in the stereotaxic frame. Afterward, the scalp of the mouse was incised, and the temporalis muscle was dissected from the skull using forceps. Tissue adhesive (3M, cat. no. 70200742529) was applied to secure the retracted muscles and incision edges, ensuring proper closure of the skin. Subsequently, a headpost was fixed to the skull using tissue adhesive and dental cement (Sun Medical Co., Ltd, cat. no. Super-Bond C&B). The skull was then carefully thinned using a high-speed rotary micromotor (Foredom, cat. no. K.1070) to create a cranial window with a width of approximately 8 mm laterally and which extending from bregma to lambda in the anterior-posterior direction. The skull was continuously thinned along this outline until it became loose, allowing for separation of the bone from the dura mater using forceps. After removing the skull, a polymethyl pentene plastic sheet (Goodfellow, cat. no. ME311051) was placed over the cranial window and fixed to the bone using tissue adhesive and dental cement. To provide protection, the window was covered with biocompatible silicone rubber (Smooth-on, cat. no. Body Double-Fast Set). Once the silicone rubber was secure, the anesthesia was discontinued, and the mouse was allowed to regain consciousness.

330 **Post-surgical care and head-fix habituation**

331 Following the surgery, subcutaneous administration of Carprofen (5-10 mg/kg body weight) was provided
332 to the animals for immediate post-operative pain management. The animals were allowed to recover from
333 anesthesia in their individual cages, with a heating pad provided to maintain optimal body temperature
334 during the recovery period. Observations were made every 15 minutes until the animals reached sternal
335 recumbency. To aid in their recovery, dry food soaked in water was provided, along with the use of recovery
336 gel (ClearH2O, cat. no. 72-06-5022) to facilitate chewing and hydration. In the case that any signs of pain
337 were observed, additional subcutaneous doses of 5-10 mg/kg Carprofen were administered every 12 to
338 24 hours to alleviate surgical discomfort for 3 days. Post-operative monitoring of the animals was
339 performed daily for a duration of 14 days following the surgery. Once the animals had fully recovered from
340 the surgical procedure, the animals were habituated daily to head fixation after walking through the body
341 tube. The duration of the head-fixation periods was gradually increased over time, starting at
342 approximately 10 minutes on day 1 and extending to up to 1 hour after 3 days[34]. If any signs of discomfort,
343 such as excessive movement or vocalization, were observed during the head-fixation sessions then the
344 sessions would be immediately discontinued.

345 **The use of 3D-printed body tube**

346 The body tube was secured to the table using four screws on the outer side, while two small screws on
347 the top were used to clamp the headpost. Two semicircular grooves that fit the size of the small screws
348 were made on the headpost (Fig. 1a). During the process of head-fixing the animal, the experimenter
349 guided the animal to enter the body tube from the rear. Once the animal protruded its head from the front
350 end, the experimenter manually grasped the headpost, gently restrained the head of the animal, and
351 subsequently aligned the semicircular grooves with the screws to immobilize the animal.

352 **Experimental procedure of imaging sessions**

353 On the day of imaging, the animal was guided to walk into the body tube, and the headpost was firmly
354 secured to the tube. The protective silicone rubber and headpost were cleaned using 70% ethanol,
355 followed by rinsing with sterile saline. Then, forceps were inserted between the silicone rubber and the
356 cement to detach the silicone rubber from the headpost. Due to the challenges of conducting continuous
357 infusion in awake animals, contrast microbubbles were administered via tail vein bolus injection in this
358 study. Animals were anesthetized with isoflurane (3% for induction and 1% for maintenance) before tail
359 vein catheterization to alleviate pain and stress. Ultrasound coupling gel was applied, and the transducer
360 was positioned to find the imaging plane. When the imaging plane was identified, the relative position of
361 the probe and the headpost was recorded, serving as a reference point for subsequent longitudinal studies.
362 B-mode and power Doppler images were also saved as references to facilitate the identification of the
363 same imaging plane in the following weeks.

364 Once the imaging plane was confirmed, the isoflurane anesthesia was terminated, and 0.1 ml of DEFINITY®
365 (Lantheus, North Billerica, MA) microbubble was administered via the tail vein catheter. The completion
366 of the injection was considered as the starting point, denoted as T = 0. From T = 0 onwards, continuous
367 ultrasound data was saved. After completion of the imaging session, the cranial window was filled with
368 the same biocompatible silicone rubber described above, allowing approximately 10 minutes for

solidification. The headpost was then removed from the body tube, and the animal was returned to its home cage. Imaging sessions were conducted once per week over a three-week period.

For the experiment of comparing differences between anesthesia and awake state (Fig. 3-5), once the mice were fixed to the body tube, they were continuously anesthetized with 2% isoflurane for more than 15 minutes. During this process, the tail vein catheterization was completed, and the imaging plane was confirmed. Following the bolus injection of 0.1 ml MB, ULM data under anesthesia was acquired for 1000 seconds. The tail vein catheter was remained in place. After the ULM acquisition under anesthesia, it was essential to wait until no bubbles were circulating within the blood stream before terminating anesthesia. Once the animal approached full arousal, another bolus injection of 0.1 ml MB was administered. The catheter was then removed, and ULM acquisition started (marked as T = 0). Other procedures were the same as those described in the previous two paragraphs. For the ULM data collected under anesthesia, since there was no specific time point at which mice achieved full pupillary dilatation, we consistently employed the RF dataset starting from T = 500s until the cumulative MB count reached 5 million for ULM reconstruction to make the MB concentration similar as in the awake cases.

Pupillary recording and measurement

Monitoring the pupillary area of rodents is commonly used to determine their level of arousal[58]. The pupils constrict under isoflurane anesthesia and enlarge upon awakening[38,59]. In this study, video recording of pupillary area performed using a camera (ace acA800-510um, Basler Inc., Exton, PA) placed in front of the mouse, with timestamps synchronized to the ultrasound acquisition. The ULM imaging session was carried out in a dark room. An infrared (IR) flashlight (EVOLVA Future Technology T20) was positioned above the camera. Since mice are functionally blind to IR wavelengths[60,61], the use of IR illumination can minimize the effect of light exposure on pupil changes so that the pupillary area is mostly influenced by anesthesia. The videos recorded by the camera were analyzed using ImageJ software, and the contour of the pupil was manually circled. The equivalent area of a single pixel was calibrated, which allowed for the quantification of the pupillary area according to the number of pixels occupied by the pupil.

Ultrasound imaging sequence

A Vantage 256 system (Verasonics Inc., Kirkland, WA) was used for this experiment. The ultrasound system was connected to a linear-array transducer (L35-16vX, Verasonics Inc.), which was fixed onto a 3D-printed holder attached to a translation motor (VT-80, Physik Instrumente, Auburn, MA). The motor allowed precise control of transducer movement in the elevational direction, enabling adjustment of the imaged coronal plane. Ultrasound was transmitted at a center frequency of 20 MHz and received at an interleaved sample rate of 125 MHz. A 9-angle compounded plane wave technique was used (angles: -8°, -6°, -4°, -2°, 0°, 2°, 4°, 6°, and 8°), with a post-compounded frame rate of 1000 Hz. The ensemble size of each dataset was 800 frames, and the acquired radiofrequency (RF) data was saved for offline reconstruction. Beamforming was conducted using the Verasonics built-in program to reconstruct the in-phase and quadrature (IQ) data. The IQ data had a pixel size of half the wavelength in the axial direction and one wavelength in the lateral direction.

ULM image processing

To ensure consistent localization of bubbles at different depths, a noise equalization method was employed to adjust signal intensity[62]. High pass filtering with a cutoff frequency of 30Hz was applied to

the IQ data to enhance sensitivity for MB extraction. MBs moving toward and away from the transducer were separated into two distinct datasets (upward flow and downward flow) based on the positive and negative Doppler shifts[40]. Subsequently, singular value decomposition (SVD) filtering was applied to the IQ data to further eliminate clutter signals from tissue and extract MB signals[63,64]. The singular value cutoff was adaptively determined to achieve objective and stable filtering results[65]. The filtered MB data was then spline interpolated to a resolution with a lateral and axial pixel size of one-tenth of the wavelength (4.928 µm). Each interpolated frame was subjected to 2D normalized cross-correlation with the point spread function of the imaging system, which was empirically determined. Regional maxima in the cross-correlation results indicated the center position of MBs[55]. Thresholding of image intensity was applied to reject low-intensity values and prevent noise from being erroneously identified as bubbles. The coordinates of the microbubble center points obtained from each frame were tracked using the uTrack algorithm[66,67]. To ensure the detection of reliable MB tracks, only tracks with a minimum length of 10 consecutive frames were considered valid. Accumulating the MB tracks resulted in the flow intensity map. The final values were square-root transformed to compress the dynamic range of the image for display. The distance traveled by MB between adjacent frames was calculated during the tracking process to determine blood flow velocity, which was then assigned to each individual bubble track. The average velocity computed from multiple tracks was used to generate a comprehensive flow speed map.

Classification of cerebral vessels

Within a small region of interest, we assume that all arteries or veins will exhibit unidirectional flow, with arteries flowing in one direction and veins flowing in the opposite direction. Capillary and microvessel flow will have a low intensity value relative to arteries/veins due to the stochastic ULM reconstruction process[39]. Therefore, an empirical threshold was applied to the ULM intensity values, regarding pixels with intensity values below 2 as “capillary” and those above 2 as either artery or vein depending on flow direction. Vessels that flow from the main vessel stem to the outer branches were classified as arteries, while vessels that flow from the branches back to the main stem were classified as veins. Flow toward the probe (upward flow) and flow away from the probe (downward flow) was determined according to the Doppler frequency shift and was used to classify artery vs. vein. For example, as shown in Fig. 4a, the vessels can be divided into upper and lower segments. Within each segment, the blood flow direction is consistent for vessels of the same type. In the lower segment, the vessels with downward flow were identified as arteries (e.g., artery 1) since they flow from the stem to the branches. Conversely, the vessels with upward flow, flowing from the branches back to the trunk, were classified as veins (e.g., vein 1).

Acknowledgements

This study was partially supported by the National Institute on Aging, the National Institute of Biomedical Imaging and Bioengineering, and the National Institute of Neurological Disorders and Stroke of the National Institutes of Health under grant numbers R21EB030072, R21EB030072-01S1, R21AG077173, R56NS131516, and by the National Science Foundation CAREER Award 2237166. The content is solely the responsibility of the authors and does not necessarily represent the official views of the NIH and NSF. MRL was supported by a Beckman Institute Postdoctoral Fellowship. We thank Dr. Baher Ibrahim and Mr. Gang Xiao from Dr. Daniel Llano’s lab for their assistance with the awake imaging setup. We thank Dr. Danqing Hu from Emory University for her insights regarding the impact of anesthetics on cerebral blood flow.

Reference

1. Bullmore, E. & Sporns, O. Complex brain networks: graph theoretical analysis of structural and functional systems. *Nat. Rev. Neurosci.* **10**, 186–198 (2009).
2. Misgeld, T. & Kerschensteiner, M. In vivo imaging of the diseased nervous system. *Nat. Rev. Neurosci.* **7**, 449–463 (2006).
3. Ji, N., Freeman, J. & Smith, S. L. Technologies for imaging neural activity in large volumes. *Nat. Neurosci.* **19**, 1154–1164 (2016).
4. Grandjean, J. *et al.* Common functional networks in the mouse brain revealed by multi-centre resting-state fMRI analysis. *NeuroImage* **205**, 116278 (2020).
5. Gutierrez-Barragan, D. *et al.* Unique spatiotemporal fMRI dynamics in the awake mouse brain. *Curr. Biol.* **32**, 631-644.e6 (2022).
6. Toyama, H. *et al.* PET imaging of brain with the β-amyloid probe, [11C]6-OH-BTA-1, in a transgenic mouse model of Alzheimer's disease. *Eur. J. Nucl. Med. Mol. Imaging* **32**, 593–600 (2005).
7. Miranda, A. *et al.* Awake ^{18}F-FDG PET Imaging of Memantine-Induced Brain Activation and Test–Retest in Freely Running Mice. *J. Nucl. Med.* **60**, 844–850 (2019).
8. Ma, Y. *et al.* Wide-field optical mapping of neural activity and brain haemodynamics: considerations and novel approaches. *Philos. Trans. R. Soc. B Biol. Sci.* **371**, 20150360 (2016).
9. Zong, W. *et al.* Miniature two-photon microscopy for enlarged field-of-view, multi-plane and long-term brain imaging. *Nat. Methods* **18**, 46–49 (2021).
10. Yao, J. *et al.* High-speed label-free functional photoacoustic microscopy of mouse brain in action. *Nat. Methods* **12**, 407–410 (2015).
11. Pang, Z. *et al.* Multi-modality photoacoustic/ultrasound imaging based on a commercial ultrasound platform. *Opt. Lett.* **46**, 4382 (2021).
12. Errico, C. *et al.* Ultrafast ultrasound localization microscopy for deep super-resolution vascular imaging. *Nature* **527**, 499–502 (2015).
13. Macé, E. *et al.* Functional ultrasound imaging of the brain. *Nat. Methods* **8**, 662–664 (2011).
14. Mace, E. *et al.* Functional ultrasound imaging of the brain: theory and basic principles. *IEEE Trans. Ultrason. Ferroelectr. Freq. Control* **60**, 492–506 (2013).
15. Deffieux, T., Demené, C. & Tanter, M. Functional Ultrasound Imaging: A New Imaging Modality for Neuroscience. *Neuroscience* **474**, 110–121 (2021).
16. Edelman, B. J. & Macé, E. Functional ultrasound brain imaging: Bridging networks, neurons, and behavior. *Curr. Opin. Biomed. Eng.* **18**, 100286 (2021).
17. Renaudin, N. *et al.* Functional ultrasound localization microscopy reveals brain-wide neurovascular activity on a microscopic scale. *Nat. Methods* **19**, 1004–1012 (2022).
18. Lowerison, M. R. *et al.* Aging-related cerebral microvascular changes visualized using ultrasound localization microscopy in the living mouse. *Sci. Rep.* **12**, 619 (2022).
19. Chavignon, A., Hingot, V., Orset, C., Vivien, D. & Couture, O. 3D transcranial ultrasound localization microscopy for discrimination between ischemic and hemorrhagic stroke in early phase. *Sci. Rep.* **12**, 14607 (2022).
20. Demené, C. *et al.* Transcranial ultrafast ultrasound localization microscopy of brain vasculature in patients. *Nat. Biomed. Eng.* **5**, 219–228 (2021).
21. Sullender, C. T., Richards, L. M., He, F., Luan, L. & Dunn, A. K. Dynamics of isoflurane-induced vasodilation and blood flow of cerebral vasculature revealed by multi-exposure speckle imaging. *J. Neurosci. Methods* **366**, 109434 (2022).
22. Masamoto, K. & Kanno, I. Anesthesia and the Quantitative Evaluation of Neurovascular Coupling. *J. Cereb. Blood Flow Metab.* **32**, 1233–1247 (2012).

23. Slupe, A. M. & Kirsch, J. R. Effects of anesthesia on cerebral blood flow, metabolism, and neuroprotection. *J. Cereb. Blood Flow Metab.* **38**, 2192–2208 (2018).
24. Reimann, H. M. & Niendorf, T. The (Un)Conscious Mouse as a Model for Human Brain Functions: Key Principles of Anesthesia and Their Impact on Translational Neuroimaging. *Front. Syst. Neurosci.* **14**, 8 (2020).
25. Aksenov, D. P., Li, L., Miller, M. J., Iordanescu, G. & Wyrwicz, A. M. Effects of Anesthesia on BOLD Signal and Neuronal Activity in the Somatosensory Cortex. *J. Cereb. Blood Flow Metab.* **35**, 1819–1826 (2015).
26. Pisauro, M. A., Dhruv, N. T., Carandini, M. & Benucci, A. Fast Hemodynamic Responses in the Visual Cortex of the Awake Mouse. *J. Neurosci.* **33**, 18343–18351 (2013).
27. Desai, M. *et al.* Mapping brain networks in awake mice using combined optical neural control and fMRI. *J. Neurophysiol.* **105**, 1393–1405 (2011).
28. Flusberg, B. A. *et al.* High-speed, miniaturized fluorescence microscopy in freely moving mice. *Nat. Methods* **5**, 935–938 (2008).
29. Guo, H., Chen, Q., Qin, W., Qi, W. & Xi, L. Detachable head-mounted photoacoustic microscope in freely moving mice. *Opt. Lett.* **46**, 6055 (2021).
30. Tang, J. *et al.* Noninvasive High-Speed Photoacoustic Tomography of Cerebral Hemodynamics in Awake-Moving Rats. *J. Cereb. Blood Flow Metab.* **35**, 1224–1232 (2015).
31. Bertolo, A. *et al.* Whole-Brain 3D Activation and Functional Connectivity Mapping in Mice using Transcranial Functional Ultrasound Imaging. *J. Vis. Exp.* 62267 (2021) doi:10.3791/62267.
32. Macé, É. *et al.* Whole-Brain Functional Ultrasound Imaging Reveals Brain Modules for Visuomotor Integration. *Neuron* **100**, 1241-1251.e7 (2018).
33. Sans-Dublanc, A. *et al.* Optogenetic fUSI for brain-wide mapping of neural activity mediating collicular-dependent behaviors. *Neuron* **109**, 1888-1905.e10 (2021).
34. Brunner, C. *et al.* Whole-brain functional ultrasound imaging in awake head-fixed mice. *Nat. Protoc.* **16**, 3547–3571 (2021).
35. Beckmann, L. *et al.* Longitudinal deep-brain imaging in mouse using visible-light optical coherence tomography through chronic microprism cranial window. *Biomed. Opt. Express* **10**, 5235 (2019).
36. Wang, Y., Liang, G., Liu, F., Chen, Q. & Xi, L. A Long-Term Cranial Window for High-Resolution Photoacoustic Imaging. *IEEE Trans. Biomed. Eng.* **68**, 706–711 (2021).
37. Tournissac, M. *et al.* Cranial window for longitudinal and multimodal imaging of the whole mouse cortex. *Neurophotonics* **9**, (2022).
38. Turner, K. L., Gheres, K. W. & Drew, P. J. Relating Pupil Diameter and Blinking to Cortical Activity and Hemodynamics across Arousal States. *J. Neurosci.* **43**, 949–964 (2023).
39. Hingot, V. *et al.* Microvascular flow dictates the compromise between spatial resolution and acquisition time in Ultrasound Localization Microscopy. *Sci. Rep.* **9**, 2456 (2019).
40. Huang, C. *et al.* Short Acquisition Time Super-Resolution Ultrasound Microvessel Imaging via Microbubble Separation. *Sci. Rep.* **10**, 6007 (2020).
41. Rakymzhan, A., Li, Y., Tang, P. & Wang, R. K. Differences in cerebral blood vasculature and flow in awake and anesthetized mouse cortex revealed by quantitative optical coherence tomography angiography. *J. Neurosci. Methods* **353**, 109094 (2021).
42. Cao, R. *et al.* Functional and oxygen-metabolic photoacoustic microscopy of the awake mouse brain. *NeuroImage* **150**, 77–87 (2017).
43. Sicard, K. *et al.* Regional Cerebral Blood Flow and BOLD Responses in Conscious and Anesthetized Rats under Basal and Hypercapnic Conditions: Implications for Functional MRI Studies. *J. Cereb. Blood Flow Metab.* **23**, 472–481 (2003).
44. Lyons, D. G., Parpaleix, A., Roche, M. & Charpak, S. Mapping oxygen concentration in the awake mouse brain. *eLife* **5**, e12024 (2016).

45. Takuwa, H. *et al.* Hemodynamic changes during somatosensory stimulation in awake and isoflurane-anesthetized mice measured by laser-Doppler flowmetry. *Brain Res.* **1472**, 107–112 (2012).
46. Iida, H., Ohata, H., Iida, M., Watanabe, Y. & Dohi, S. Isoflurane and Sevoflurane Induce Vasodilation of Cerebral Vessels via ATP-sensitive K+Channel Activation. *Anesthesiology* **89**, 954–960 (1998).
47. Santisakultarm, T. P. *et al.* Two-photon imaging of cerebral hemodynamics and neural activity in awake and anesthetized marmosets. *J. Neurosci. Methods* **271**, 55–64 (2016).
48. Hlushchuk, R. *et al.* Innovative high-resolution microCT imaging of animal brain vasculature. *Brain Struct. Funct.* **225**, 2885–2895 (2020).
49. Kirst, C. *et al.* Mapping the Fine-Scale Organization and Plasticity of the Brain Vasculature. *Cell* **180**, 780-795.e25 (2020).
50. Dorr, A., Sled, J. G. & Kabani, N. Three-dimensional cerebral vasculature of the CBA mouse brain: A magnetic resonance imaging and micro computed tomography study. *NeuroImage* **35**, 1409–1423 (2007).
51. Xiong, B. *et al.* Precise Cerebral Vascular Atlas in Stereotaxic Coordinates of Whole Mouse Brain. *Front. Neuroanat.* **11**, 128 (2017).
52. Ghanavati, S., Lerch, J. P. & Sled, J. G. Automatic anatomical labeling of the complete cerebral vasculature in mouse models. *NeuroImage* **95**, 117–128 (2014).
53. McCall, J. R., Santibanez, F., Belgharbi, H., Pinton, G. F. & Dayton, P. A. Non-invasive transcranial volumetric ultrasound localization microscopy of the rat brain with continuous, high volume-rate acquisition. *Theranostics* **13**, 1235–1246 (2023).
54. Heiles, B. *et al.* Ultrafast 3D Ultrasound Localization Microscopy Using a 32 × 32 Matrix Array. *IEEE Trans. Med. Imaging* **38**, 2005–2015 (2019).
55. Song, P. *et al.* Improved Super-Resolution Ultrasound Microvessel Imaging With Spatiotemporal Nonlocal Means Filtering and Bipartite Graph-Based Microbubble Tracking. *IEEE Trans. Ultrason. Ferroelectr. Freq. Control* **65**, 149–167 (2018).
56. Hurst, J. L. & West, R. S. Taming anxiety in laboratory mice. *Nat. Methods* **7**, 825–826 (2010).
57. Gouveia, K. & Hurst, J. L. Optimising reliability of mouse performance in behavioural testing: the major role of non-aversive handling. *Sci. Rep.* **7**, 44999 (2017).
58. Privitera, M. *et al.* A complete pupillometry toolbox for real-time monitoring of locus coeruleus activity in rodents. *Nat. Protoc.* **15**, 2301–2320 (2020).
59. Kum, J. E., Han, H.-B. & Choi, J. H. Pupil Size in Relation to Cortical States during Isoflurane Anesthesia. *Exp. Neurobiol.* **25**, 86–92 (2016).
60. Breuninger, T., Puller, C., Haverkamp, S. & Euler, T. Chromatic Bipolar Cell Pathways in the Mouse Retina. *J. Neurosci.* **31**, 6504–6517 (2011).
61. Chang, L., Breuninger, T. & Euler, T. Chromatic Coding from Cone-type Unselective Circuits in the Mouse Retina. *Neuron* **77**, 559–571 (2013).
62. Song, P., Manduca, A., Trzasko, J. D. & Chen, S. Noise Equalization for Ultrafast Plane Wave Microvessel Imaging. *IEEE Trans. Ultrason. Ferroelectr. Freq. Control* **64**, 1776–1781 (2017).
63. Demene, C. *et al.* Spatiotemporal Clutter Filtering of Ultrafast Ultrasound Data Highly Increases Doppler and fUltrasound Sensitivity. *IEEE Trans. Med. Imaging* **34**, 2271–2285 (2015).
64. Baranger, J. *et al.* Adaptive Spatiotemporal SVD Clutter Filtering for Ultrafast Doppler Imaging Using Similarity of Spatial Singular Vectors. *IEEE Trans. Med. Imaging* **37**, 1574–1586 (2018).
65. Song, P., Manduca, A., Trzasko, J. D. & Chen, S. Ultrasound Small Vessel Imaging With Block-Wise Adaptive Local Clutter Filtering. *IEEE Trans. Med. Imaging* **36**, 251–262 (2017).
66. Jaqaman, K. *et al.* Robust single-particle tracking in live-cell time-lapse sequences. *Nat. Methods* **5**, 695–702 (2008).
67. Stein, S. C. & Thiart, J. TrackNTrace: A simple and extendable open-source framework for developing single-molecule localization and tracking algorithms. *Sci. Rep.* **6**, 37947 (2016).

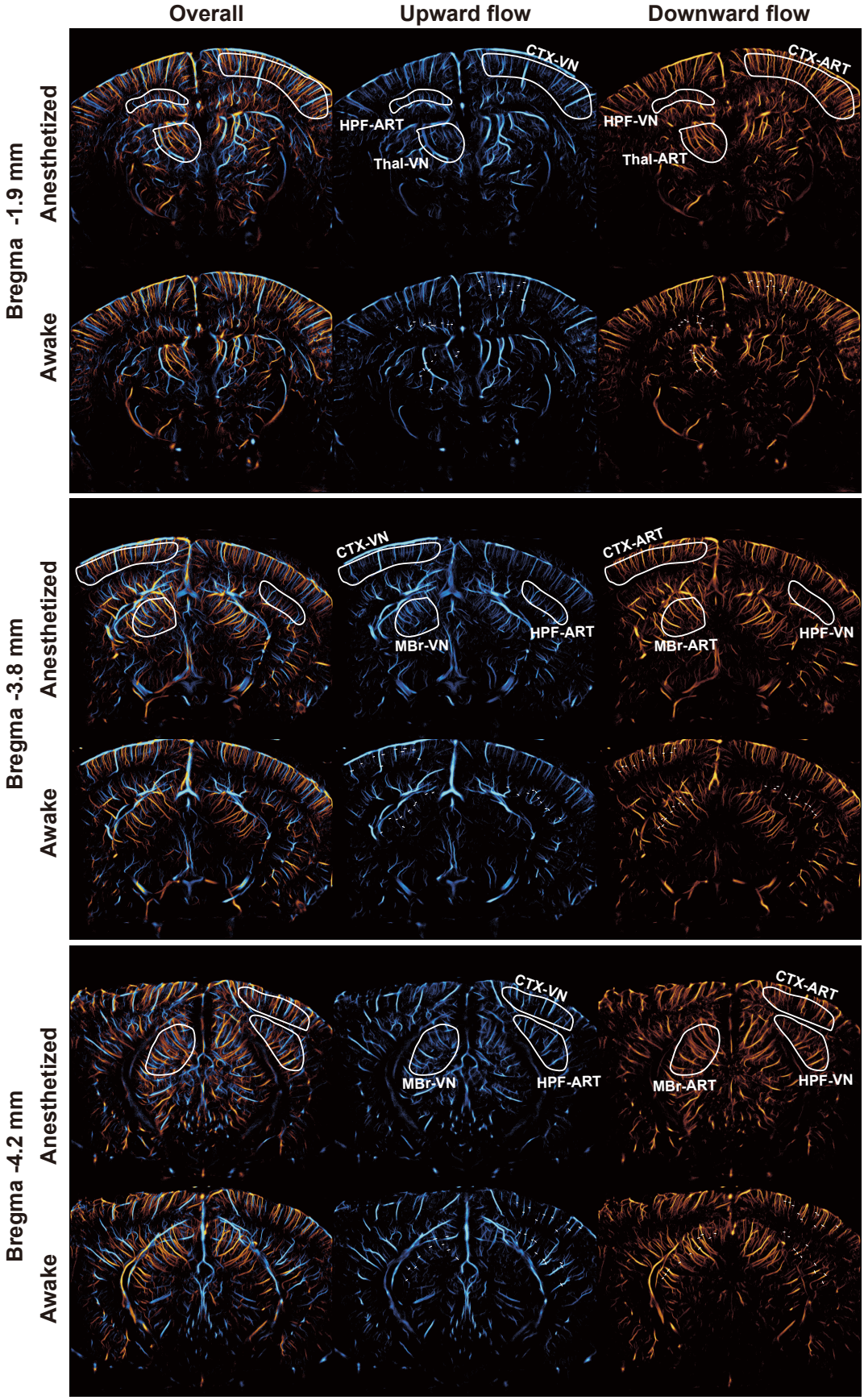

591 **Supplementary Fig. 1 | Comparison of ULM directional vessel density map, with the upward and downward flow separately depicted.** In the entire coronal section of the brain, the upward flow of vessels includes both arteries and veins, so as to the downward flow. However, within a small region of interest (ROI), blood flow in the same direction can be regarded as the same type of vessel. Based on this assumption, three ROIs from the cortex, hippocampus, and brainstem respectively are delineated in each plane. Ten arteries and ten veins from each brain region are selected (white profile across the vessel) to calculate diameter change in Fig. 5. ART: artery, VN: vein, CAP: capillary, CTX: cortex, HPF: hippocampus formation, Thal: Thalamus, MBr: Midbrain.